Monthly Notices of the ROYAL ASTRONOMICAL SOCIETY

MNRAS **531,** 2213–2222 (2024) https://doi.org/10.1093/mnras/stae1251
Advance Access publication 2024 May 14

An antihalo void catalogue of the Local Super-Volume

Stephen Stopyra [1]★ Hiranya V. Peiris [1,2] Andrew Pontzen,[3] Jens Jasche[1] and Guilhem Lavaux[4]

[1]*The Oskar Klein Centre for Cosmoparticle Physics, Department of Physics, Stockholm University, AlbaNova, Stockholm SE-106 91, Sweden*
[2]*Institute of Astronomy and Kavli Institute for Cosmology, University of Cambridge, Madingley Road, Cambridge CB3 0HA, UK*
[3]*Department of Physics and Astronomy, University College London, Gower Street, London WC1E 6BT, UK*
[4]*Sorbonne Université, CNRS, UMR 7095, Institut d'Astrophysique de Paris, F-75014 Paris, France*

Accepted 2024 May 8. Received 2024 April 11; in original form 2023 December 4

ABSTRACT

We construct an antihalo void catalogue of 150 voids with radii $R > 10\,h^{-1}$ Mpc in the Local Super-Volume ($< 135\,h^{-1}$ Mpc from the Milky Way), using posterior resimulation of initial conditions inferred by field-level inference with Bayesian Origin Reconstruction from Galaxies (BORG). We describe and make use of a new algorithm for creating a single, unified void catalogue by combining different samples from the posterior. The catalogue is complete out to $135\,h^{-1}$ Mpc, with void abundances matching theoretical predictions. Finally, we compute stacked density profiles of those voids which are reliably identified across posterior samples, and show that these are compatible with Λ cold dark matter expectations once environmental selection (e.g. the estimated ~ 4 per cent underdensity of the Local Super-Volume) is accounted for.

Key words: methods: data analysis – large-scale structure of Universe – cosmology: theory.

1 INTRODUCTION

Cosmic voids – regions of the Universe with significantly lower density than the clusters and filaments where most galaxies are found – make up the majority of the Universe's volume, and provide a pristine environment for probing cosmology and fundamental physics (Kirshner et al. 1981; Zeldovich, Einasto & Shandarin 1982). In particular, the shapes of voids, via their ellipticity distribution (Park & Lee 2007) or the Alcock–Paczynski test (Alcock & Paczynski 1979), and their abundance via the void size function, can be used to constrain cosmological parameters (Sutter et al. 2012, 2014; Contarini et al. 2023). Furthermore, voids can probe modifications to General Relativity on large scales which may be hidden by screening in denser areas of the Universe (Spolyar, Sahlén & Silk 2013; Joyce et al. 2015), and probe the dark energy equation of state (Lee & Park 2009).

However, there are a large number of different void definitions in use. A commonly used empirical approach is to identify voids from the morphology of the density or galaxy field via the watershed algorithm, using codes such as ZOBOV (Neyrinck 2008) or VIDE (Sutter et al. 2015). Other approaches include spherical voids (Padilla, Ceccarelli & Lambas 2005; Ceccarelli et al. 2006; Ruiz et al. 2015), and the related popcorn voids (Paz et al. 2023). Most of these definitions use the present day galaxy distribution, which traces the underlying dark matter, and the morphology of the cosmic web. This makes the relationship between cosmological initial conditions and the shapes, sizes, and abundance of voids challenging to model, in contrast with haloes where the relationship can be understood via excursion set models (Bond et al. 1991) and modifications thereof. Several authors have studied the abundance of voids with similar excursion-set approaches (Sheth & van de Weygaert 2004; Jennings, Li & Hu 2013), but it has proven challenging to relate these calculations to observational data (Nadathur & Hotchkiss 2015).

One approach in which the abundance can be directly predicted, however, is the *antihalo* model of voids, proposed by Pontzen et al. (2016), and further studied by Stopyra, Peiris & Pontzen (2021b), Shim et al. (2021, 2023), and Desmond et al. (2022). In the antihalo approach, voids in an N-body simulation are defined in analogy to clusters by performing an 'anti-universe' simulation with density-inverted initial conditions: by exchanging underdense and overdense regions in the initial conditions, particles identified as belonging to haloes in the anti-universe simulation correspond to voids in the original simulation. The abundance of such voids is then directly related to the initial conditions via the (anti-)halo mass function, placing haloes and antihalo voids on equal footing.

Because antihaloes are defined with reference to structure formation theory, identifying them in observational data requires additional steps. Shim et al. (2023) used an approach with Gaussian smoothing to infer the locations of antihaloes from galaxy data, calibrated using simulations and mock galaxy catalogues. To construct an antihalo catalogue directly from the dark matter density field, one would require access to the initial conditions of an N-body simulation which, when evolved forward, corresponds to the actual density field of the present-day Universe. Field-level inference is an ideal approach for achieving this, since it can be used to sample the posterior distribution of possible initial conditions conditioned on the observed galaxy distribution. The Bayesian Origin Reconstruction from Galaxies (BORG) algorithm (Jasche & Lavaux 2019) is one such example of field-level inference. By utilizing the *posterior resimulation*

★ E-mail: stephen.stopyra@fysik.su.se

technique (Stopyra et al. 2023, hereafter S23), i.e. resimulating samples and density-reversed samples from the posterior distribution, and identifying antihalo voids in each sample, it is possible to build an ensemble of samples from the posterior distribution of antihalo catalogues.

Recently, Desmond et al. (2022) built an antihalo void catalogue based on initial conditions derived from the Markov chain produced by Jasche & Lavaux (2019). However, it was subsequently demonstrated by S23 that the forward model used for field-level inference by Jasche & Lavaux (2019) was insufficiently accurate to describe massive haloes (and antihaloes). This led to an overestimate of antihalo masses and therefore, an overestimate of the antihalo mass function (see S23).

In this work, we present an antihalo catalogue for voids in the Local Super-Volume using posterior resimulations of initial conditions from a new Markov chain computed by S23, based on Bayesian Origin Reconstruction from Galaxies (BORG; Jasche & Wandelt 2013) applied to the 2M++ galaxy catalogue (Lavaux & Hudson 2011). This chain uses a 20-step COLA (Tassev, Zaldarriaga & Eisenstein 2013) forward model to increase the accuracy of initial condition inference relative to earlier work by Jasche & Lavaux (2019), eliminating the aforementioned spurious excess of antihaloes seen by Desmond et al. (2022). We also introduce an algorithm for combining lists of antihaloes from different posterior resimulations into a combined catalogue of well-constrained voids, robustly identified across the different posterior samples.

The structure of this paper is as follows: In Section 2, we explain how field-level inference with BORG can be used to produce an ensemble of antihalo lists via resimulation of posterior samples, and then outline our algorithm for combining these lists into a single, unified void catalogue. In Section 3, we compare the abundance of voids in the combined catalogue to Λ cold dark matter (ΛCDM) predictions using the antihalo mass function and void size function, and also compute the stacked void density profile. We discuss the implications of these results for the compatibility of the Local Super-Volume with ΛCDM in Section 4.

2 METHODS

In this work, we make use of the technique of posterior resimulation (see S23) in order to link the antihalo void definition with data, and thereby construct a void catalogue from the 2M++ galaxy survey (Lavaux & Hudson 2011). We begin by briefly outlining the posterior resimulation technique and describing how we selected $N = 20$ posterior samples for resimulation in Section 2.1. Using methods outlined in Section 2.2, we use these posterior resimulations to construct 20 lists of antihaloes, one for each posterior sample. In Section 2.3, we show how to combine these samples into a single catalogue of robustly identified voids. We then describe how to construct the stacked void profile of this combined catalogue in Section 2.4.

2.1 Posterior resimulation with BORG

The central technique in this work will be *posterior resimulation*, as presented in our recent work, S23. The approach uses field-level inference to draw samples from the posterior distribution of possible initial conditions compatible with data (in this case, the 2M++ galaxy catalogue of the Local Super-Volume). These initial conditions can then be evolved to redshift $z = 0$ using an N-body solver. We can also evolve a 'reversed' set of initial conditions, in which the density contrast is inverted (swapping underdensities and overdensities); this allows antihalo catalogues to be generated for each sample.

The first crucial ingredient in reliable posterior resimulation is that the accuracy of the field-level inference is sufficient to accomplish the science goals. For our present purposes, it is vital to reproduce the halo and antihalo mass function accurately within resimulations. S23 studied the required accuracy in the gravity solver which, during the inference process, is by necessity approximate; we found that it is possible to balance computational speed with physical accuracy, even to the point of obtaining reliable mass estimates of individual clusters. The same level of accuracy was shown to be sufficient for voids, we therefore use results from the same Markov chain, obtained with a 20-step COLA gravity solver, in this work. The inference makes use of the Neyrinck et al. (2014) bias model, which describes galaxy bias as a power law with an exponential cutoff in order to allow for different behaviour in underdense regions. See S23 for further details on why an approximate gravity solver can lead to convergence on cluster and void masses via posterior resimulation.

A second crucial ingredient is that the structures being resimulated (clusters, or voids) are reliably represented across posterior samples, more frequently than is found by cross-matching objects in independent, random simulations. This is because the posterior contains a mix of prior-driven and data-constrained structures. To reliably identify the latter, it is necessary to establish that their frequency of occurrence in posterior samples is significantly more likely than by chance alone. We discuss this requirement and its implementation in practice in Section 2.3.

The 20 samples used in this work were drawn from the Markov Chain Monte Carlo (MCMC) chain computed by S23. Balancing available computational resources and the fact that the MCMC samples are correlated, we picked a subsample for resimulation which saturates the available statistical power in constraining structures in the relevant mass range. The samples were chosen from the portion of the chain after burn in, with a spacing of 300 samples between every sample which was resimulated. This spacing was chosen since it was longer than the correlation lengths of all the relevant model parameters of the field-level inference, as well as the correlation lengths of the density field around the largest clusters (see S23 for further details). We further investigated the effect of doubling the number of samples from 10 to 20 on the catalogue, finding that this did not lead to significant changes in the catalogue. We now describe the use of these 20 samples for posterior resimulation.

The posterior resimulations contain 512^3 particles over a $677.7\,h^{-1}$ Mpc box, evolved to $z = 0$ from the inferred initial conditions with GADGET2 (Springel 2005). While BORG produces a 256^3 output, we interpolate this to 512^3 for resimulation so that shot noise can be suppressed for the largest haloes. Density-reversed initial conditions are created using `genetIC` (Stopyra et al. 2021a) and also evolved to $z = 0$ to provide reverse (anti-universe) simulations for generating antihaloes. We also run 20 independent random simulations (with both forward and reverse initial conditions for each) with the same settings, but random initial conditions, to use as a ΛCDM reference. Random initial conditions are generated on a 256^3 grid and interpolated up to a 512^3 grid with `genetIC` in order to replicate the procedure used for posterior resimulation and account for any differences arising from the interpolation step. Throughout this work, we use the Planck 2018 cosmological parameters (Planck Collaboration VI 2020), with lensing and baryon acoustic oscillations: $\Omega_\mathrm{m} = 0.3111$, $\sigma_8 = 0.8102$, $H_0 = 67.66\,\mathrm{km\,s^{-1}\,Mpc^{-1}}$, $n_\mathrm{s} = 0.9665$, $\Omega_\mathrm{b} = 0.049$.

2.2 Identifying antihaloes in posterior resimulations

To identify antihaloes from posterior resimulations, we apply the halo finder AHF (Knollmann & Knebe 2009) to the reverse simulations. The particles corresponding to each halo in the reverse simulation are then mapped to the corresponding particles in the forward simulation, where they define the antihaloes. We compute a Voronoi tessellation using the VOBOZ code (Neyrinck, Gnedin & Hamilton 2005) in order to assign every particle i in the antihalo a volume, V_i. We then compute for each antihalo the volume-weighted centre, $\boldsymbol{x}_{\rm VW}$, and effective radius, $r_{\rm eff}$, given by

$$x_{\rm VW} = \frac{1}{V}\sum_i V_i x_{\rm i}, \tag{1}$$

$$r_{\rm eff} = \left(\frac{3V}{4\pi}\right)^{1/3}, \tag{2}$$

where i runs over all particles in the antihalo and $V = \sum_i V_i$ is the total volume of all Voronoi cells. The impact of redshift space distortions is already taken into account during the inference step in Section 2.1. We refer the reader to S23 for more details, but in brief the gravity solver is used to model velocities at each point, which allows the density field to be computed in redshift space for comparison with galaxy catalogue data. Applied to each resimulation, this gives us $N = 20$ separate lists of antihaloes (independent samples from the posterior distribution), which we now combine to create a single robust antihalo catalogue.

2.3 Construction of the antihalo catalogue

The constraining power of the galaxy catalogue is variable within the volume that it samples, due to signal-to-noise fluctuations in the data. Therefore some antihaloes identified in the previous step are expected to be well-constrained by data and stable across the $N = 20$ independent posterior resimulations, while others will not be reproduced across the samples. In addition, even those which are present in each sample will differ in varying degrees as to their exact locations and radii. Therefore, creating a combined catalogue requires us to associate these slightly differing antihaloes found in different resimulations with a single, reliably reproducible void. A method for identifying candidates for the 'same' halo between resimulated posterior samples has been proposed by Hutt et al. (2022) and recently Stiskalek et al. (2023) have proposed an approach based on the overlap of Lagrangian regions. However, for reliable posterior resimulation it is necessary to assess how well-constrained an individual cluster or void is by the data, as opposed to being largely prior driven. This can be quantified by defining a *reproducibility score*, defined as the fraction of posterior samples in which a void appears, and comparing with independent random catalogues to assess whether a match is significantly more likely than chance.

Our primary desiderata for creating a combined antihalo catalogue are:

(i) The catalogue should prioritize reliability and reproducibility over completeness;
(ii) Each posterior sample should be on an equal footing, i.e. antihaloes identified in any one resimulation should not be privileged over those from another resimulation;
(iii) Those antihaloes appearing in the combined catalogue should closely agree in their centres and radii across a high fraction of the resimulations.

In order to address desideratum (i), we filter the antihaloes identified in each resimulation based on thresholds for signal to noise and minimum radius corresponding to the resolution limit of the simulations. We only seek to include voids in the final catalogue with radii $r_{\rm eff}$ above 10 h^{-1} Mpc, which corresponds approximately to the minimum mass at which haloes can be resolved with least 100 particles in posterior resimulations. However, to avoid edge effects, we perform the matching with smaller voids down to $5\,h^{-1}$ Mpc, and retain only voids with mean radii above $R > 10\,h^{-1}$ Mpc after matching. In order to apply the signal-to-noise cut, we remove antihaloes for which the mean value of $(\delta/\sigma_\delta)^2$ over the voxels within a sphere of radius $r_{\rm eff}$ about an antihalo's centre is less than 10, where δ is the mean density contrast over all MCMC samples in a voxel, and σ_δ the standard deviation of the density contrast over a voxel.

The above procedure yields 20 filtered lists of antihaloes which we pass on to an iterative matching procedure as follows. We start by initializing a candidate list of voids using the centres and effective radii from one of the resimulations, which we denote as resimulation 1. We then match these candidates with the antihaloes in resimulation 2 by demanding that the centre and radii are equal within a specified threshold. This introduces two parameters which reflect the tolerance on the location and radius matches, respectively. We call these tolerance parameters μ_S and μ_R for the centre and radius, respectively.

In practice, these must scale with the size of the voids being matched, and we therefore express them as dimensionless fractions of the radius. Since the antihalo radius may differ from the radius of the candidate void, the search radius tolerance, μ_S, is defined as the ratio of the maximum permitted distance between the centres of the voids to the geometric mean between their radii. The radius ratio is defined as the *minimum* allowed ratio between the lowest radius and highest radius void in a pair. Explicitly, consider a pair of voids with centres $\boldsymbol{x_1}, \boldsymbol{x_2}$, and radii R_1, R_2, respectively. Assuming that $R_1 < R_2$ without loss of generality, the radius ratio and search distance ratio must satisfy

$$\mu_R \leq \frac{R_1}{R_2} \leq 1, \tag{3}$$

$$\mu_S \geq \frac{|x_1 - x_2|}{\sqrt{R_1 R_2}} \geq 0. \tag{4}$$

If more than one antihalo in resimulation 2 satisfies our criteria for a given candidate void, we flag the match as ambiguous and treat it as though no match were found. Otherwise, the matching procedure is repeated starting from the antihalo list from resimulation 2 and matching it back to the candidate void list. Any antihaloes where this backwards map results in a different identification are again flagged as ambiguous, and treated as though there was no match at all. In summary, a candidate void is only treated as identified in resimulation 2 if there is a unique two-way match on to an antihalo, addressing desideratum (iii).

Once the matching of the candidate void list on to resimulation 2 is complete, the procedure begins again with resimulation 3, and so on. At this point, one may calculate the reproducibility score for each candidate void, reflecting how many of the N independent resimulations it appears within. Candidate voids with a high reproducibility score are more robust than those with a low-reproducibility score, and we will shortly return to how we threshold the candidate voids on this robustness measure.

However, at this point in the algorithm, the candidate void list has unfairly privileged resimulation 1 over the other $N - 1 = 19$ resimulations, in contradiction with our desideratum (ii). There is therefore the need to iterate the candidate void list, replacing its initial centres and radii with the mean over all antihaloes counted as a match. We find that typical candidate voids converge to a

single shared centre and radius within a few iterations, but any which do not converge within 100 iterations are discarded as unreliable.[1]

In order to choose the values of μ_R and μ_S in practice, we made use of a visually confirmed 'curated set' of voids which are found with high confidence in a high fraction of the void lists obtained from the 20 posterior resimulations. The curated set of voids consisted of 30 voids selected by hand which were verified by visual inspection to have corresponding voids in more than half of samples. We inspected the spread of centres and radii of these curated voids and chose $\mu_R = 0.75$, $\mu_S = 0.5$ as accurately identifying unique matches for this curated void set while yielding as tight a tolerance as possible on antihalo centres and radii across the resimulations. This value of μ_R corresponds to allowing radii to differ by no more than 25 per cent with respect to the larger radius in a pair, while the chosen value of μ_S means that void centres can differ from each other by no more than half the geometric mean of their radii. We explored the parameter space of possible values around this canonical set of parameters to confirm that this choice recovered the curated voids while also producing a final catalogue with high completeness.

After this stage, it is necessary to impose a reproducibility score cut in order to remove poorly constrained voids from the catalogue. This cut must be carefully chosen in a radius-dependent manner in order to obtain a pure catalogue. We carried out the following procedure to minimize the possibility of spurious voids making it into the combined catalogue via chance alignments. First, we applied the algorithm specified above to a set of antihalo lists created from 20 independent, random simulations. For both this random catalogue and the combined catalogue obtained from the posterior resimulations, we then computed the reproducibility score of each void. We observed that the threshold for a significant reproducibility score was radius dependent: smaller voids would frequently be matched by chance in random catalogues, while this was rarer for larger voids. To allow for this, we binned both catalogues in seven bins by the void mean radius, equally spaced between 10–20 h^{-1} Mpc, and removed all voids in the combined catalogue whose reproducibility score was lower than the 99th percentile for the same bin in the random catalogue. These bins were chosen since they subdivide the radius range as much as possible, while also yielding at least $\sim O(1)$ voids in even the highest radius bins. We checked that changing the binning scheme does not significantly affect the catalogue as long as more than three radius bins are used. The reproducibility score for each void is given in Table A1. The threshold reproducibility scores as a function of radial bin are given in Table A2. Overall, the reproducibility score cut removes 44 per cent of the voids above 10 h^{-1} Mpc in the combined catalogue obtained in the previous step.

We use this filtered set as our final catalogue. We estimate the properties of each void in the final catalogue – such as the mean centre, effective radius, and central density – as the mean of that property over the corresponding antihaloes in each posterior resimulation in which it is found. We provide the reproducibility score and signal to noise of each void as a measure of the void's reliability.

[1]In practice, this did not affect any of the voids above 10 h^{-1} Mpc in our experiments, but we retain this stop condition so that the algorithm will not become stuck if handling less well-constrained and/or smaller voids.

2.4 Computation of void density profiles

The void dark matter density profile as a function for radius is sensitive to changes in the cosmology (Dai 2015; Chantavat et al. 2016), deviations from the standard laws of gravity in low-density regions (Falck et al. 2018), and the effects of neutrinos (Schuster et al. 2019; Contarini et al. 2021). It is, however, not directly observable, and typically the galaxy number density profile is used instead (Hamaus, Sutter & Wandelt 2014; Nadathur et al. 2015; Schuster et al. 2023). An innovation in our work is that the dark matter distribution has been inferred and can be used to construct a stacked (i.e. averaged) dark matter density profile from our combined final catalogue, as described below.

We first estimate the density profile for each void by averaging across the antihaloes matched to it within the posterior resimulations. Specifically, we construct spherical shells around the volume-weighted centre in equation (1) for each MCMC sample and use the total mass of dark matter particles in each to obtain a density estimate using a volume-weighted mean, as outlined by Nadathur et al. (2015), but taken over the N realizations of the *same* void in all samples. The uncertainty on each individual void profile (with index i) is calculated by computing the variance, $\sigma_i^2(r)$, of this profile over all samples. These density estimates are then averaged between the individual antihaloes to obtain a final estimate for the void density profile as a function of the scaled radius, $r/r_{\rm eff}$.

We then stack these posterior profiles across the entire catalogue, again following the volume-weighted stacking procedure of Nadathur et al. (2015). Since we use dark matter particles rather than galaxy tracers, Poisson errors are subdominant to profile variability and we therefore use a different procedure to that used by Nadathur et al. (2015) to compute the uncertainty in the stacked profile. This procedure is outlined in Stopyra et al. (2021b) and gives the variance, $\sigma^2_{\rm mean}(r)$, of the volume-weighted mean profile in a stack, $\rho_{\rm mean}(r)$, as

$$\sigma^2_{\rm mean}(r) = \left(\sum_i w_i^2\right)\sigma^2(r), \tag{5}$$

where we sum over all voids, i, in the stack with volume-weights $w_i = V_i/\sum_i V_i$ for void volume V_i, and $\sigma^2(r) = \mathrm{var}(\{\rho_1(r), \ldots, \rho_N(r)\})$ is the variance of all profiles in the stack and thus common to all voids. This generalizes the usual variance of the mean for weighted means, and reduces to $\sigma^2(r)/N$ for the case of N equal weights.

However, because each void in the stack now has a significant uncertainty associated with it, quantified by the variability of the profile of this specific void across the 20 MCMC samples, the procedure requires a slight modification. We add the variance of the profile mean with the posterior variances of each void in the stack, $\sigma_i^2(r)$, to obtain

$$\sigma^2_{\rm profile}(r) = \sum_i w_i^2\left(\sigma^2(r) + \sigma_i^2(r)\right). \tag{6}$$

Equation (6) then gives the final error bar on the stacked profile, in each radial bin.

To obtain a ΛCDM profile to compare with, we apply the same stacking procedure to antihaloes within the random simulations previously described (though in this case there is no posterior variance on each individual void profile). In order to construct a fair comparison, we need to account for several environmental selection effects related to the properties of the Local Super-Volume. The Local Super-Volume voids exist within an underdense region of the Universe (the mean density contrast over all MCMC samples

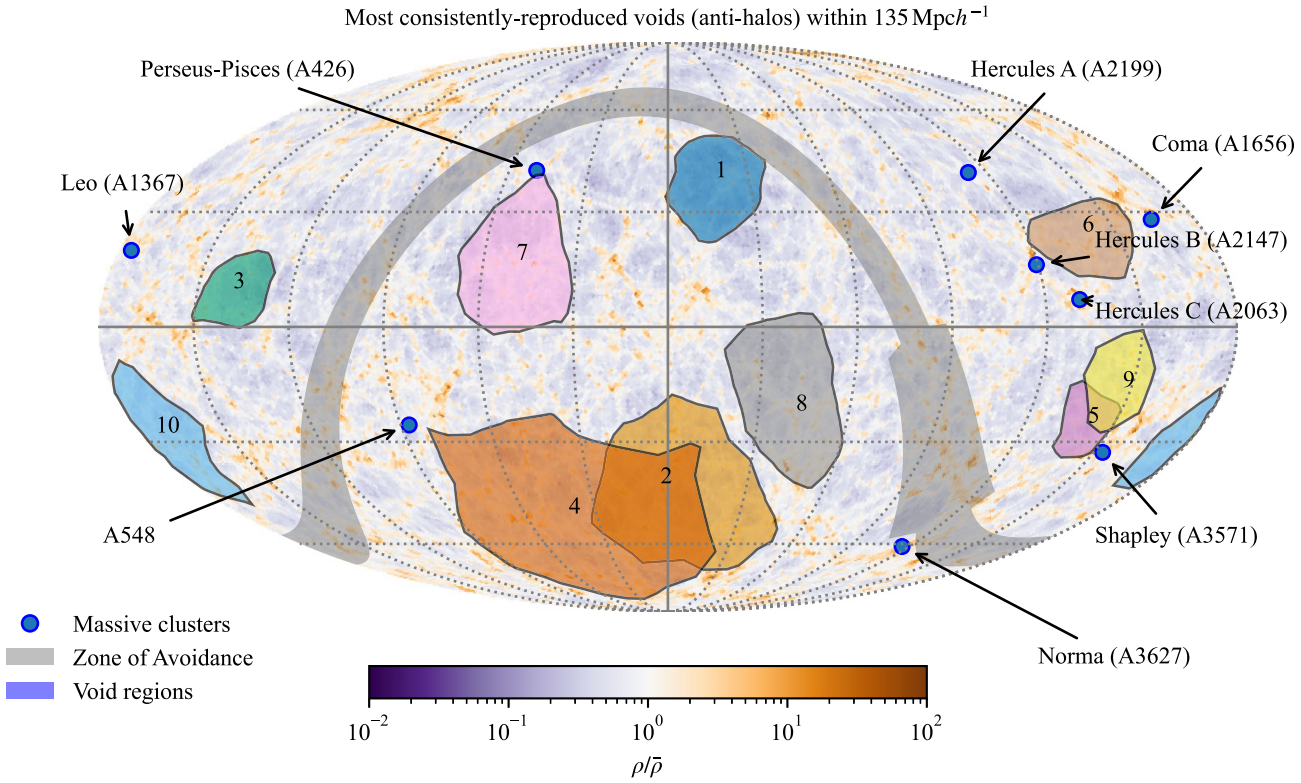

Figure 1. Projected locations of the 10 antihalo voids which appear most consistently across 20 MCMC samples (all have reproducibility scores of 0.95 or above). Numbers follow the same ordering as in Table A1, sorted in descending order of reproducibility score. Voids 1–6 appear in all 20 posterior resimulations, while voids 7–10 are each missing in only 1 of 20 samples. Note that apparent void sizes are driven by distance-dependent projection effects.

is $\delta = -0.043 \pm 0.001$), and their central and average void density distributions (defined as the density within 1/4 of the void radius, and the total mass divided by the total volume of the void, respectively) form subsets of void properties that occur within ΛCDM simulations sampling all environments. To account for these selection effects, our comparison profiles are constructed from antihaloes found within 135 h^{-1} Mpc spheres with a density contrast matched to that of the Local Super-Volume [in this case, choosing regions whose density contrast lies within a 68 per cent confidence interval of the maximum a posteriori (MAP) estimate, $\delta_{\rm MAP} = -0.041$[2]]. We randomly select voids from these matched regions in a way that (up to the limits of sample size within each region) reproduces as closely as possible the central/average density distribution of the combined catalogue. To avoid duplication, we retain only spherical regions that do not overlap, giving a total of 144 density-matched regions over 20 random simulations. Finally, we compute the mean and standard deviation of the stacked density profiles in each of the 144 regions, to compare with the combined catalogue profile. Note that there may remain additional environmental selection effects to be accounted for; however we expect the above considerations to capture the main factors.

3 RESULTS

We present the results for our combined catalogue, obtained from the set of 20 posterior samples previously described. The resulting combined catalogue consists of 150 voids with radii $> 10\,h^{-1}$ Mpc within the Local Super-Volume ($135\,h^{-1}$ Mpc of the Milky Way).

A sample of the pure set of antihaloes with high signal to noise and which are consistently represented across MCMC samples is given in Table A1 in Appendix A, with the full catalogue available online as supplementary material. We also display the locations of the most robust of these antihaloes on the sky in Fig. 1: the outlines show alpha-shapes (Edelsbrunner, Kirkpatrick & Seidel 1983) around the particles corresponding to each antihalo when projected on to the sky in a representative MCMC sample from the 20 used to construct the catalogue. Outlines are broadly similar in the other samples, but fluctuate at a minor level as matter moves around due to unconstrained modes. Note that nearby antihaloes appear larger due to projection effects.

We performed additional checks on the catalogue, including randomly permuting the order in which catalogues were processed. This led to minimal variation in the voids found.

3.1 Antihalo mass functions and void size function

In the antihalo model of voids, the abundance of voids is predicted by the halo mass function. For large radius voids ($> 10\,h^{-1}$ Mpc), the effect of crushing of voids by surrounding large-scale structure is negligible (Pontzen et al. 2016a), and so the expected abundance of voids as a function of antihalo mass can be given by any model for predicting halo mass functions, such as the Tinker mass function (Tinker et al. 2008).

We show the antihalo mass function for the combined catalogue in Fig. 2, finding that it is consistent with the ΛCDM predictions from

[2]The difference between the MAP estimate and the mean density contrast is due to the fact that the posterior on the Local Super-Volume density is non-Gaussian, and skewed.

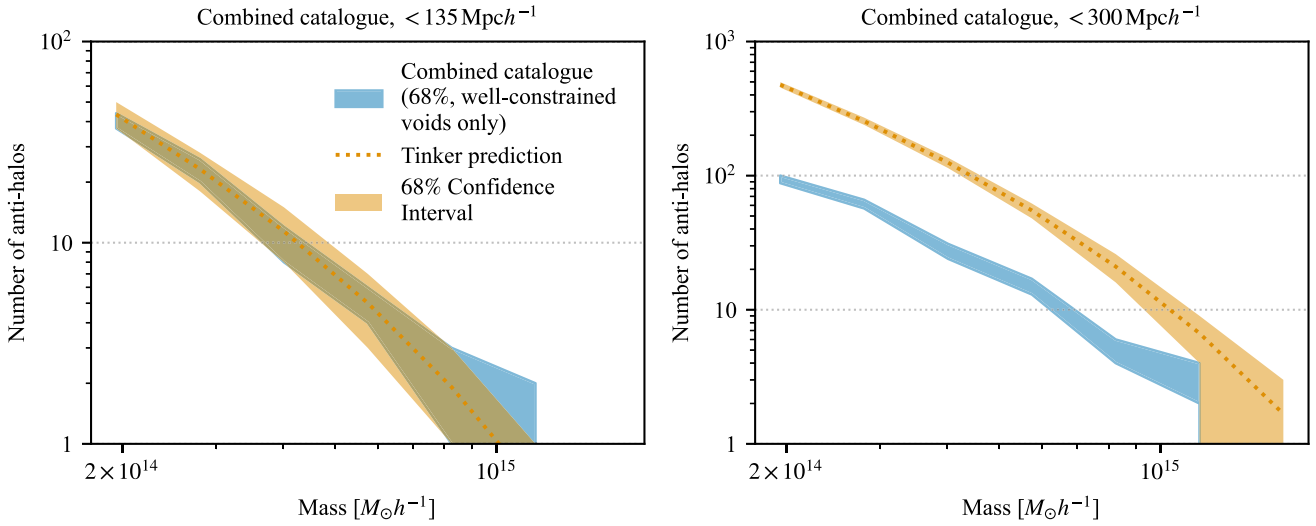

Figure 2. Mass functions for the combined catalogue of high-confidence voids. Left: voids within $135\,h^{-1}$ Mpc. The signal to noise for these is high, and the catalogue is complete for the most massive antihaloes (above $4 \times 10^{15}\,\mathrm{M}_\odot\,h^{-1}$), matching the expected number from ΛCDM predictions. Low-mass, low-radius voids tend to be more prior-driven than higher mass voids, and the algorithm therefore excludes them at a higher rate. Right: all voids within $300\,h^{-1}$ Mpc. This catalogue is largely incomplete, since there are not many more voids at this distance which can be identified with sufficient signal to noise to rule out spurious alignment between MCMC realizations. We estimate the bin count and its error using a bootstrap approach (see Section 3.1).

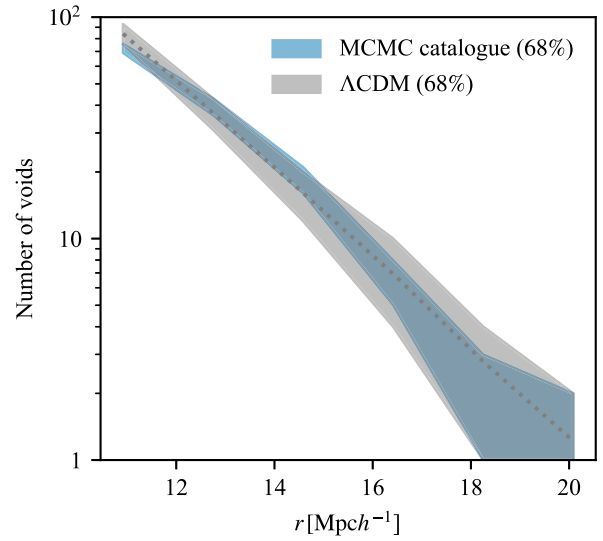

Figure 3. Void size function for the catalogue compared with the ΛCDM expectation, showing consistency across all mass bins and demonstrating the completeness of the catalogue for $> 10\,h^{-1}$ Mpc voids within $135\,h^{-1}$ Mpc of the Milky Way. As in Fig. 2, we compute a weighted histogram using the scheme outlined in Section 3.1.

the Tinker mass function within the Local Super-Volume. Looking further out to $300\,h^{-1}$ Mpc, we see that the completeness of the catalogue is much lower, an effect primarily driven by the low signal to noise further from the Milky Way. Since voids are commonly presented in the literature in the form of the void size function, we also show the abundance of voids within the Local Super-Volume as a function of their radius in Fig. 3.

To compute the uncertainty for the bin counts in each mass or radius bin, we treat the counts as a weighted histogram, with weights given by the probability that the mean lies in each bin. We estimate the probability, p_{ij}, that void i lies in bin j by bootstrapping the posterior samples to approximate the distribution of the mean mass or radius. Since a void can be either in or out of a bin, the contribution of each void to a bin is a Bernoulli-distributed variable (1 with probability p_{ij}, 0 with probability $1 - p_{ij}$). The mean bin count, n_j, and its variance then follow from the sum of N Bernoulli-distributed variables:

$$n_j = \sum_{i=1}^{N} p_{ij}, \tag{7}$$

$$\mathrm{var}(n_j) = \sum_{i=1}^{N} p_{ij}(1 - p_{ij}), \tag{8}$$

where N is the total number of voids in the catalogue (150). For large numbers of voids in a bin, n_j is approximately Gaussian. However, for the purposes of computing an accurate error bar in low-count bins we estimate the 68 per cent interval for bin counts in Figs. 2 and 3 using Monte-Carlo realizations in which each void occupies bin j with probability p_{ij}.

3.2 Void density profiles

We present the void density profiles computed using the procedure outlined in Section 2.4. Without any constraints on the voids in random ΛCDM simulations, the MCMC profiles appear to be outside the 68 per cent interval of profiles (Fig. 4, left-hand panel). However, this is driven in large part by the underdensity of the Local Super-Volume. Selecting only 144 regions of radius $135\,h^{-1}$ Mpc whose density matches that of the Local Super-Volume brings the profiles into better agreement by lowering the profile at large distances from the void centre, illustrating the influence of a void's environment on its density profiles. Even better agreement is obtained (Fig. 4, right-hand panel) when we sample a subset of voids from each region whose distribution of central and average densities match that of the Local Super-Volume, indicating consistency with ΛCDM expectations for voids in the Local Super-Volume.

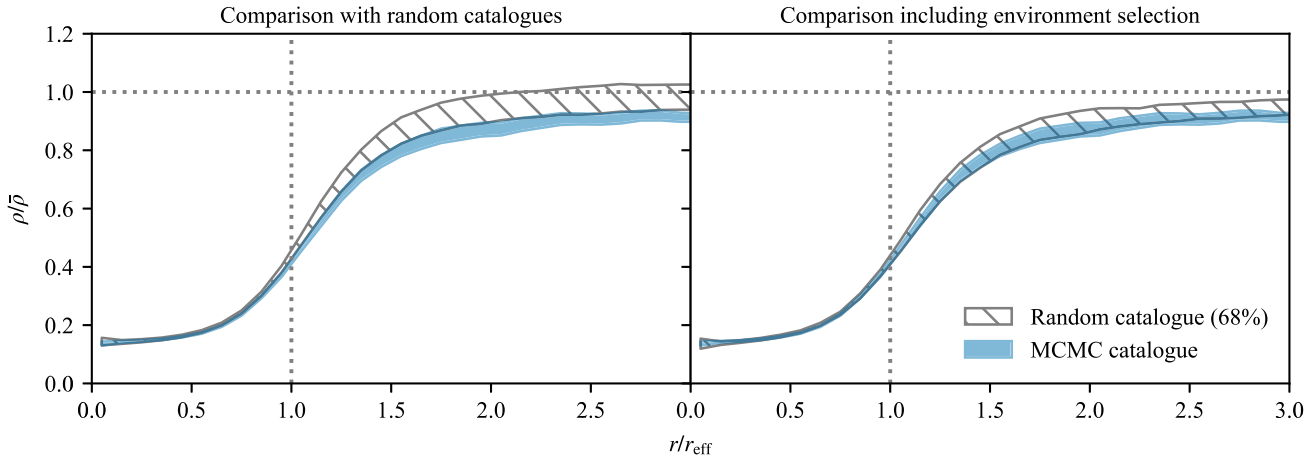

Figure 4. Density profile for the catalogue within 135 h^{-1} Mpc (shaded) compared with the 68 per cent interval for the distribution of profiles in randomly selected 135 h^{-1} Mpc regions assuming ΛCDM (solid lines with cross-hatching). Without accounting for environmental effects (left) the density between 1 and 3 effective radii in the posterior catalogue is low at the 1σ level. However, if we select regions from ΛCDM simulations which agree with the ~ 4 per cent underdensity of the Local Super-Volume (right), and additionally account for the distribution of central and average densities (see Section 2.4) the profile is consistent with ΛCDM expectations.

4 DISCUSSION

The abundance of voids, as shown in Figs 2 and 3, is consistent with ΛCDM within 135 h^{-1} Mpc. Further out, fewer voids are identified (Fig. 2, right panel), but this is consistent with expectations from signal-to-noise considerations: fewer higher signal-to-noise voids are available further out to be matched by the catalogue combination algorithm, and those that are found have lower reproducibility score. Our approach thus correctly excludes random, coincidental alignments of voids which are driven by the prior, rather than the data.

This illustrates that our approach by design creates a very pure catalogue, which can be used for high-precision tests of cosmology. The completeness of the catalogue at higher redshifts is primarily limited by the availability of high-tracer-density, high-precision redshift data. Therefore, there is broad scope to build larger catalogues of high-quality voids, by including Sloan Digital Sky Survey (SDSS; Abazajian et al. 2009) data, and data from upcoming surveys such as *Euclid* (Laureijs et al. 2011; Scaramella et al. 2022), the Vera Rubin Observatory's Legacy Survey of Space and Time (Ivezić et al. 2019), the Roman Space Telescope's High Latitude Survey (Wenzl et al. 2022), the Dark Energy Spectroscopic Instrument (DESI; DESI Collaboration et al. 2022), and the Spectro-Photometer for the History of the Universe, Epoch of Reionization, and Ices Explorer (Doré et al. 2014). Fully exploiting the mix of photometric and spectroscopic data in next-generation surveys will however require careful analysis to account for differences in tracer density and redshift precision (Jasche & Wandelt 2012). The 2M++ results we present in this work, however, already build a robust picture of the voids in the Local Super-Volume.

Although we assume a ΛCDM prior with fixed cosmological parameters in the inference (Section 2.1), the high-signal-to-noise regions are demonstrably data driven. Direct evidence of this for the central 135 h^{-1} Mpc region can be seen in the left panel of Fig. 2: by construction, 99 per cent of prior-driven voids would be discarded by our reproducibility score cut, but the abundance of voids we actually see is consistent with ΛCDM. Where the signal-to-noise ratio drops (beyond 135 h^{-1} Mpc), our catalogue strongly favours incompleteness over returning spurious prior-driven voids (right panel of Fig. 2).

We expect our catalogue to be insensitive to the ΛCDM prior used in the inference. BORG seeks to reproduce the final density field, and therefore the void centres and radii are strongly constrained by data. Adopting a different set of cosmological parameters would primarily change the power spectrum, while the locations of void regions are primarily determined by phase information. Such information has previously been shown to be insensitive to cosmological assumptions (Villaescusa-Navarro et al. 2020; Kostić et al. 2022). However, detailed features such as the density profiles may show stronger cosmological dependencies. It would therefore be of clear interest to explore the impact of sampling over cosmological parameters or models (Porqueres et al. 2022; Andrews et al. 2023). A full investigation will be the subject of future work.

4.1 Influence of the environment on void density profiles

It is clear from our results (Fig. 4) that environmental selection impacts the shape of the (stacked) void density profile. The primary factor driving these results is the fact that the Local Super-Volume density is lower than the cosmological average at the 68 per cent level ($\delta_{\rm MAP} = -0.041 \pm 0.001$, bootstrap error). Accounting for this environmental effect explains the low value of the profile compared to a ΛCDM 'average' profile, and the finer details of the profile are consistent with ΛCDM once the distribution of central and average void densities in the catalogue is also accounted for.

Previous studies of voids have indicated a universal void density profile that is found to apply across a wide array of void sizes (Hamaus et al. 2014; Nadathur et al. 2015) and redshifts (Nadathur et al. 2014). This remains true of antihalo void stacks when averaging over all environments, but our results highlight the importance of the environment of cosmic voids in shaping their density profiles. This manifests foremost in the large-radius profile returning to a lower background density (see Fig. 4, right-hand panel). However, we also see dependence on the profile on the average density of voids. This highlights that in addition to information about gravitational evolution, void profiles contain information about the larger-scale environment in which a void is found. Conversely, this indicates that the environment in which voids are found must be self-

consistently accounted for when comparing void catalogues with cosmological models.

4.2 Comparison to watershed void catalogues

Leclercq et al. (2015) built a watershed void catalogue for the SDSS using BORG and the void-finding code VIDE (Sutter et al. 2015) and Leclercq et al. (2017) examined more general cosmic web classifiers, including voids. Leclercq et al. (2015) also performed simulations of posterior samples, an approach they refer to as non-linear filtering, which shares similarities to the posterior resimulation approach we use in this work, but lacks an object-by-object matching. As such, while they were able to estimate aggregate properties of their void catalogue with a Blackwell–Rao approach, it was not possible to study the reliability of individual voids. By contrast, posterior resimulation requires satisfying accuracy requirements on field level inference (S23), and an assessment of the reliability of the structures appearing in resimulated posterior samples (this work).

There is an effective limit of ~ 25–$30\,h^{-1}$ Mpc on the radius an antihalo void can have, due to the absence of significant number of haloes above $10^{15}\,\mathrm{M}_\odot\,h^{-1}$. Higher radius voids are frequently found in other void catalogues such as GIGANTES (Kreisch et al. 2022), and other catalogues based on the Baryon Oscillation Spectroscopic Survey (BOSS) Data Release 12 (DR12) data such as the watershed catalogues by Nadathur (2016) and Mao et al. (2017). However, these typically represent shallower, large-volume voids which in the antihalo picture would not yet have virialized. Particles within such watershed voids are typically found within smaller antihaloes in analogy to the bottom-up picture of structure formation with haloes – see Pontzen et al. (2016) for example.

4.3 Concluding remarks

We have presented a void catalogue for the Local Super-Volume, constructed by robustly combining antihalo voids identified in posterior resimulations of the dark matter density field using initial conditions obtained with field-level inference. The methodology used to construct the catalogue is general and can be applied to posterior resimulations of field-level inferred initial conditions for any galaxy catalogue.

Our catalogue is complete out to $135\,h^{-1}$ Mpc, identifying all antihaloes with radii $> 10\,h^{-1}$ Mpc. We have shown that it is compatible with ΛCDM expectations, both in the abundance of voids, and in the shape of the stacked void density profiles. One application of the catalogue, which we leave to future work, is to constrain cosmological effects whose impact is strongly felt in low-density regions. An important example is neutrino masses, which are known to impact the abundance of voids (Kreisch et al. 2019), and their density profiles (Massara et al. 2015). Additionally, modified gravity models such as $f(R)$ (Hu & Sawicki 2007) and nDGP (Dvali, Gabadadze & Porrati 2000) theories are known to affect the shapes of voids and their density profiles (Cai, Padilla & Li 2014; Cautun et al. 2018; Falck et al. 2018; Paillas et al. 2019). While such theories are heavily constrained in their ability to explain dark energy (Saridakis et al. 2021), cosmological constraints are still capable of constraining the properties of gravity itself (Shankaranarayanan & Johnson 2022). A challenge which remains, however, is how to disentangle the effects of modified gravity from that of massive neutrinos, since both have similar effects on void density profiles (Baldi et al. 2014; Hagstotz et al. 2019).

In future work, we will explore the impact on the detailed properties of voids within the catalogue, if one assumes different cosmologies within field-level inference. These developments will be crucial for obtaining robust constraints on gravity, cosmology, and particle physics using the Local Super-Volume. In the meantime, however, we will test the consistency of the local void population with ΛCDM predictions, an important first step enabled by the catalogue of voids presented in this work.

ACKNOWLEDGEMENTS

We thank Metin Ata, Harry Desmond, Stuart McAlpine, and Daniel Mortlock for useful discussions regarding this work. This project received funding from the European Research Council (ERC) under the European Union's Horizon 2020 research and innovation programmes (grant agreement no. 101018897 CosmicExplorer and 818085 GMGalaxies). This work has been enabled by support from the research project grant 'Understanding the Dynamic Universe' funded by the Knut and Alice Wallenberg Foundation under Dnr KAW 2018.0067. SS and HVP are additionally supported by the Göran Gustafsson Foundation for Research in Natural Sciences and Medicine. HVP and JJ acknowledge the hospitality of the Aspen Center for Physics, which was supported by National Science Foundation grant PHY-1607611. The participation of HVP and JJ at the Aspen Center for Physics was supported by the Simons Foundation. JJ acknowledges support by the Swedish Research Council (VR) under the project 2020-05143 – 'Deciphering the Dynamics of Cosmic Structure' and by the Simons Collaboration on 'Learning the Universe'. This work was partially enabled by the UCL Cosmoparticle Initiative. The computations/data handling were enabled by resources provided by the Swedish National Infrastructure for Computing (SNIC) at Linköping University, partially funded by the Swedish Research Council through grant agreement no. 2018-05973. This research also utilized the Sunrise HPC facility supported by the Technical Division at the Department of Physics, Stockholm University. This work was carried out with support from the Aquila Consortium.[3]

DATA AVAILABILITY

The data underlying this article will be shared on reasonable request to the corresponding author. The full combined catalogue in Table A1 is supplied as supplementary material in csv format. Additional data, including the antihalo catalogues for each MCMC sample, is available on Zenodo at https://doi.org/10.5281/zenodo.10160612.

REFERENCES

Abazajian K. N. et al., 2009, ApJS, 182, 543
Alcock C., Paczynski B., 1979, Nature, 281, 358
Andrews A., Jasche J., Lavaux G., Schmidt F., 2023, MNRAS, 520, 5746
Baldi M., Villaescusa-Navarro F., Viel M., Puchwein E., Springel V., Moscardini L., 2014, MNRAS, 440, 75
Bond J. R., Cole S., Efstathiou G., Kaiser N., 1991, ApJ, 379, 440
Cai Y.-C., Padilla N., Li B., 2014, Proc. Int. Astron. Union, 11, 555
Cautun M., Paillas E., Cai Y.-C., Bose S., Armijo J., Li B., Padilla N., 2018, MNRAS, 476, 3195
Ceccarelli L., Padilla N. D., Valotto C., Lambas D. G., 2006, MNRAS, 373, 1440
Chantavat T., Sawangwit U., Sutter P. M., Wandelt B. D., 2016, Phys. Rev. D, 93, 043523

[3] https://aquila-consortium.org

Contarini S., Marulli F., Moscardini L., Veropalumbo A., Giocoli C., Baldi M., 2021, MNRAS, 504, 5021
Contarini S., Pisani A., Hamaus N., Marulli F., Moscardini L., Baldi M., 2023, ApJ, 953, 46
Dai D.-C., 2015, MNRAS, 454, 3590
DESI Collaboration, 2022, AJ, 164, 207
Desmond H., Hutt M. L., Devriendt J., Slyz A., 2022, MNRAS, 511, L45
Doré O. et al., 2014, preprint (arXiv:1412.4872)
Dvali G., Gabadadze G., Porrati M., 2000, Phys. Lett. B, 484, 112
Edelsbrunner H., Kirkpatrick D., Seidel R., 1983, IEEE Trans. Inform. Theory, 29, 551
Falck B., Koyama K., Zhao G.-B., Cautun M., 2018, MNRAS, 475, 3262
Hagstotz S., Gronke M., Mota D. F., Baldi M., 2019, A&A, 629, A46
Hamaus N., Sutter P., Wandelt B. D., 2014, Phys. Rev. lett., 112, 251302
Hu W., Sawicki I., 2007, Phys. Rev. D, 76, 064004
Hutt M. L., Desmond H., Devriendt J., Slyz A., 2022, MNRAS, 516, 3592
Ivezić, Ž. et al., 2019, ApJ, 873, 111
Jasche J., Lavaux G., 2019, A&A, 625, A64
Jasche J., Wandelt B. D., 2012, MNRAS, 425, 1042
Jasche J., Wandelt B. D., 2013, MNRAS, 432, 894
Jennings E., Li Y., Hu W., 2013, MNRAS, 434, 2167
Joyce A., Jain B., Khoury J., Trodden M., 2015, Phys. Rep., 568, 1
Kirshner R. P., Oemler A. J., Schechter P. L., Shectman S. A., 1981, ApJ, 248, L57
Knollmann S. R., Knebe A., 2009, ApJS, 182, 608
Kostić A., Jasche J., Ramanah D. K., Lavaux G., 2022, A&A, 657, L17
Kreisch C. D., Pisani A., Carbone C., Liu J., Hawken A. J., Massara E., Spergel D. N., Wandelt B. D., 2019, MNRAS, 488, 4413
Kreisch C. D., Pisani A., Villaescusa-Navarro F., Spergel D. N., Wandelt B. D., Hamaus N., Bayer A. E., 2022, ApJ, 935, 100
Laureijs R. et al., 2011, preprint (arXiv:1110.3193)
Lavaux G., Hudson M. J., 2011, MNRAS, 416, 2840
Leclercq F., Jasche J., Sutter P., Hamaus N., Wandelt B., 2015, J. Cosmol. Astropart. Phys., 2015, 047
Leclercq F., Jasche J., Lavaux G., Wandelt B., Percival W., 2017, J. Cosmol. Astropart. Phys., 2017, 049
Lee J., Park D., 2009, ApJ, 696, L10
Mao Q. et al., 2017, ApJ, 835, 161
Massara E., Villaescusa-Navarro F., Viel M., Sutter P., 2015, J. Cosmol. Astropart. Phys., 2015, 018
Nadathur S., 2016, MNRAS, 461, 358
Nadathur S., Hotchkiss S., 2015, MNRAS, 454, 2228
Nadathur S., Hotchkiss S., Diego J., Iliev I., Gottlöber S., Watson W., Yepes G., 2014, Proc. Int. Astron. Union, 11, 542
Nadathur S., Hotchkiss S., Diego J., Iliev I., Gottlöber S., Watson W., Yepes G., 2015, MNRAS, 449, 3997
Neyrinck M. C., 2008, MNRAS, 386, 2101
Neyrinck M. C., Gnedin N. Y., Hamilton A. J., 2005, MNRAS, 356, 1222
Neyrinck M. C., Aragón-Calvo M. A., Jeong D., Wang X., 2014, MNRAS, 441, 646
Padilla N. D., Ceccarelli L., Lambas D. G., 2005, MNRAS, 363, 977
Paillas E., Cautun M., Li B., Cai Y.-C., Padilla N., Armijo J., Bose S., 2019, MNRAS, 484, 1149
Park D., Lee J., 2007, Phys. Rev. Lett., 98, 081301
Paz D. J., Correa C. M., Gualpa S. R., Ruiz A. N., Bederián C. S., Graña R. D., Padilla N. D., 2023, MNRAS, 522, 2553
Planck Collaboration VI, 2020, A&A, 641, A6
Pontzen A., Slosar A., Roth N., Peiris H. V., 2016, Phys. Rev. D, 93, 103519
Porqueres N., Heavens A., Mortlock D., Lavaux G., 2022, MNRAS, 509, 3194
Ruiz A. N., Paz D. J., Lares M., Luparello H. E., Ceccarelli L., Lambas D. G., 2015, MNRAS, 448, 1471
Saridakis E. N., Lazkoz R., Salzano V., Moniz P. V., Capozziello S., Jiménez J. B., De Laurentis M., Olmo G. J., 2021, Modified Gravity and Cosmology. Springer-Verlag, Berlin
Scaramella R. et al., 2022, A&A, 662, A112
Schuster N., Hamaus N., Pisani A., Carbone C., Kreisch C. D., Pollina G., Weller J., 2019, J. Cosmol. Astropart. Phys., 2019, 055
Schuster N., Hamaus N., Dolag K., Weller J., 2023, J. Cosmol. Astropart. Phys., 2023, 031
Shankaranarayanan S., Johnson J. P., 2022, Gen. Relativ. Gravit., 54, 44
Sheth R. K., van de Weygaert R., 2004, MNRAS, 350, 517
Shim J., Park C., Kim J., Hwang H. S., 2021, ApJ, 908, 211
Shim J., Park C., Kim J., Hong S. E., 2023, Eur. Phys. J. C, 83, 1095
Spolyar D., Sahlén M., Silk J., 2013, Phys. Rev. lett., 111, 241103
Springel V., 2005, MNRAS, 364, 1105
Stiskalek R., Desmond H., Devriendt J., Slyz A., 2023, preprint (arXiv:2310.20672)
Stopyra S., Pontzen A., Peiris H., Roth N., Rey M. P., 2021a, ApJS, 252, 28
Stopyra S., Peiris H. V., Pontzen A., 2021b, MNRAS, 500, 4173
Stopyra S., Peiris H. V., Pontzen A., Jasche J., Lavaux G., 2023, MNRAS, 527, 1244
Sutter P. M., Lavaux G., Wandelt B. D., Weinberg D. H., 2012, ApJ, 761, 187
Sutter P., Pisani A., Wandelt B. D., Weinberg D. H., 2014, MNRAS, 443, 2983
Sutter P. et al., 2015, Astron. Comput., 9, 1
Tassev S., Zaldarriaga M., Eisenstein D. J., 2013, J. Cosmol. Astropart. Phys., 2013, 036
Tinker J. L., Kravtsov A. V., Klypin A., Abazajian K., Warren M. S., Yepes G., Gottlober S., Holz D. E., 2008, ApJ, 688, 709
Villaescusa-Navarro F. et al., 2020, ApJS, 250, 2
Wenzl L., Doux C., Heinrich C., Bean R., Jain B., Doré O., Eifler T., Fang X., 2022, MNRAS, 512, 5311
Zeldovich Y. B., Einasto J., Shandarin S., 1982, Nature, 300, 407

SUPPORTING INFORMATION

Supplementary data are available at *MNRAS* online.

Table A1. First 10 of 150-total voids in the antihalo catalogue for voids within 135 h^{-1} Mpc.
Please note: Oxford University Press is not responsible for the content or functionality of any supporting materials supplied by the authors. Any queries (other than missing material) should be directed to the corresponding author for the article.

APPENDIX A: THE ANTIHALO CATALOGUE

In Table A1, we present the final catalogue after applying the combination algorithm in Section 2.3. Uncertainties are computed as the standard deviation of the mean over all antihaloes matching to a given void (which may not include all samples if a void is missing in some samples). The voids are sorted by the reproducibility score, which quantifies how robustly a void appears in all catalogues (a reproducibility score of 1 indicates that a void appeared in all catalogues). As discussed in Section 2.3, voids with reproducibility scores not significantly higher than would be found by chance alone are not included. We also show the reproducibility score thresholds for each radius bin in Table A2.

Table A1. First 10 of 150-total voids in the antihalo catalogue for voids within 135 h^{-1} Mpc. Radii and mass uncertainties are computed as the standard error on the mean over the antihaloes in each MCMC sample matching on to a given void. The signal-to-noise ratio (SNR) is the mean signal to noise for each of the same contributing antihaloes, computed as the average of δ^2/σ_δ^2 as discussed in Section 2.3. The voids are sorted by reproducibility score, defined as the fraction of MCMC samples which contain a representative antihalo for a given void. The entire catalogue is provided as supplementary material.

ID	Radius (h^{-1} Mpc)	Mass ($10^{14}\,h^{-1}\,M_\odot$)	R.A. (deg.)	Dec. (deg.)	z	Distance (h^{-1} Mpc)	SNR	Reproducibility score
1	21 ± 0.3	9.5 ± 0.4	343	37.2	0.026	113	18.3	1
2	14 ± 0.2	3 ± 0.2	0.263	−39.9	0.01	45.1	147	1
3	17 ± 0.3	5.1 ± 0.2	139	8.68	0.031	135	21.3	1
4	14 ± 0.2	3.2 ± 0.2	40.6	−50.2	0.0072	32	23.7	1
5	11 ± 0.2	1.4 ± 0.07	218	−25.6	0.021	93.7	79.2	1
6	13 ± 0.1	2.5 ± 0.09	223	24.1	0.018	79.2	147	1
7	13 ± 0.1	2 ± 0.07	49.6	14.5	0.011	48	42.2	0.95
8	11 ± 0.2	1.6 ± 0.08	318	−19.7	0.0097	42.7	35	0.95
9	10 ± 0.2	1.2 ± 0.09	212	−14.4	0.017	74.3	44.6	0.95
10	11 ± 0.2	1.5 ± 0.06	174	−28.6	0.012	52.4	30	0.95

Table A2. Reproducibility score thresholds in each radius bin, above which 99 per cent of voids in ΛCDM simulations are excluded.

Radius bin range (h^{-1} Mpc)	Reproducibility score threshold
10–11.4	0.2
11.4–12.9	0.2
12.9–14.3	0.15
14.3–15.7	0.15
15.7–17.1	0.15
17.1–18.6	0.142
18.6–20	0.1

This paper has been typeset from a TEX/LATEX file prepared by the author.